Plasmon-Coupled Gold Nanoparticles in Stretched Shape-Memory Polymers for Mechanical/Thermal Sensing

Prachi R. Yadav, Mehedi H. Rizvi, Björn Kuttich, Sumeet R. Mishra, Brian S. Chapman, Brian B. Lynch, Tobias Kraus, Amy L. Oldenburg, and Joseph B. Tracy*

ABSTRACT: The organization of plasmonic nanoparticles (NPs) determines the strength and polarization dependence of coupling of their surface plasmons. In this study, plasmon coupling of spherical Au NPs with an average diameter of 15 nm was investigated in shape-memory polymer films before and after mechanical stretching and then after thermally driving shape recovery. Clusters of Au NPs form when preparing the films that exhibit strong plasmon coupling. During stretching, a significant polarization-dependent response develops, where the optical extinction maximum corresponding to the surface plasmon resonance is redshifted by 19 nm and blueshifted by 7 nm for polarization parallel and perpendicular to the stretching direction, respectively. This result can be explained by non-uniform stretching on the nanoscale, where plasmon coupling increases parallel to the shear direction as Au NPs are pulled into each other during stretching. The polarization dependence vanishes after shape recovery, and structural characterization confirms the return of isotropy consistent with complete nanoscale recovery of the initial arrangement of Au NPs. Simulations of the polarized optical responses of Au NP dimers at different interparticle spacings establish a plasmon ruler for estimating the average interparticle spacings within the experimental samples. An investigation of the temperature-dependent recovery behavior demonstrates an application of these materials as optical thermal history sensors.

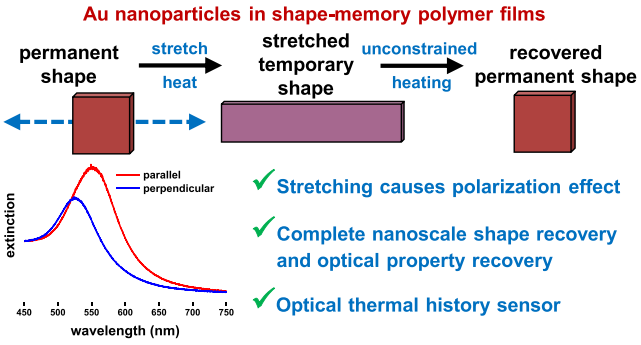

KEYWORDS: *gold, nanoparticles, surface plasmon resonance, plasmon coupling, shape-memory polymer, polymer nanocomposite, temperature sensor, strain sensor*

INTRODUCTION

Polymer nanocomposite thin films containing functional nanoparticles (NPs) are a rich and complex system, where the organization of the NPs can determine their properties based on their orientation or coupling.[1−10] When plasmonic NPs, such as Au NPs, are dispersed within or assembled on the surfaces of polymer films, their organization determines the interparticle distances and extent of coupling of their surface plasmon resonances (SPRs).[11−23] Therefore, nanocomposites based on elastomers and shape-memory polymers (SMPs) are of special interest, where there is a capability to alter the spacing between NPs and thereby control the optical properties of the thin film. Plasmonic elastomer and SMP nanocomposites have a wide range of potential applications, including sensors, optoelectronics, and optical filters.[24−29]

SMPs are a diverse class of polymers with temporary shapes that can be programmed by stretching or bending and maintained until recovery of the permanent shape is triggered with external stimuli, most commonly, temperature.[30−32] Applying one-way, thermally activated SMPs involves a four-step process that can be repeated, where the polymer is (i) programmed into a temporary shape via externally applied forces while heating above its transition temperature, (ii) cooled below the transition temperature to room temperature, which locks the temporary shape, (iii) released from external forces, and (iv) heated above the transition temperature to recover the permanent shape. For this study, we have selected a commercially available thermoplastic polyurethane (TPU) polymer, Diaplex MM5520, which has a glass transition temperature of ~55 °C.[33,34] In a recent study using Diaplex, we showed that photothermal heating of embedded Au NPs can be used to optically trigger shape recovery of bent, thin films of the nanocomposite.[35] Here, we have investigated stretching of the same type of film containing embedded Au NPs, with a focus on the optical properties and how they

change when the film is stretched into a temporary shape and then recovers its permanent shape after thermal heating. As the organization of the Au NPs in Diaplex changes during heating, stretching, and shape recovery, polarization-dependent shifts in the optical extinction spectra indicate altered coupling of the surface plasmons. We note that extinction can have contributions from both absorption and scattering processes. For the size of Au NPs employed in this study, with an average diameter of 15 nm, minimal scattering is anticipated, and absorption is the dominant type of interaction with light. The small contributions of scattering were also included in our simulations for consistency with experimental measurements of the extinction.

Coupling of the surface plasmons of noble metal NPs is well established for the development of sensors that provide an optical readout of molecular and biological phenomena. Plasmon coupling has allowed for the development of plasmon rulers[36,37] and is employed in surface-enhanced Raman spectroscopy.[38] There is significant interest in controlling the assembly or aggregation of NPs into clusters and then adjusting the properties of the clusters dynamically with chemical, optical, and thermal stimuli.[39] Use of SMPs for the matrix provides a simple way of mechanically controlling and manipulating the assembly of the NPs.

It is well established that stretching polymer films containing embedded plasmonic NPs can impart polarization-dependent optical properties, where spherical and rod-shaped Au and Ag NPs have been the most widely studied. Shearing during stretching tends to align nanorods with the stretching direction, causing an increase in the red optical extinction peak corresponding to the longitudinal SPR for light polarized parallel to the stretching direction. For light polarized perpendicular to the stretching direction, this peak disappears, and there is a corresponding increase in the bluer peak corresponding to the transverse SPR.[22,40−45] Obtaining polarized extinction from spherical plasmonic NPs requires anisotropy in their local environment, for example, due to coupling with other NPs in dimers or larger clusters. Stretching composites containing clusters of spherical NPs commonly results in a redshift in the polarized optical extinction parallel to the stretching direction and a blueshift perpendicular to the stretching direction,[46−49] in agreement with the results we report here, but shifts in the opposite directions have also been reported.[13]

If clusters of NPs dispersed within a polymer would be uniformly pulled along with the polymer in the stretching direction and uniformly compressed perpendicular to the stretching direction, then decoupling of the plasmons and blueshifting would be expected when measuring the extinction parallel to the stretching direction, and redshifting would be expected perpendicular to the stretching direction. The reverse trend is usually observed, which may be attributed to morphological effects determined by the polymer and the surface functionalization of the NPs that do not allow uniform movement of NPs. Some of the NPs may be pinned, and other NPs may be pulled into them along the stretching direction. While the Poisson effect still occurs, compressing the NPs along the perpendicular direction, the more significant result of clustering along the stretching direction prevails.

Most previous studies of stretching polymer composites with embedded plasmonic NPs have employed poly(vinyl alcohol) (PVA), which is an SMP, and silicone elastomers. To the best of our knowledge, the effects of shape recovery of SMPs with embedded plasmonic NPs on the optical properties of the composite have not been investigated previously. Rather, prior studies of SMPs have utilized embedded plasmonic NPs for photothermal heating to control shape recovery.[35,45,50−56] Use of an SMP matrix enables integration of the polarization-dependent optical properties obtained through shearing with shape memory.

In this work, polarized extinction spectra of stretched Diaplex films indicate a change in the coupling among the NPs. The capability to relate mechanical strain to the optical properties and the conditions for shape recovery can be applied for combined mechanical/thermal sensors. Scanning electron microscopy (SEM) and small-angle X-ray scattering (SAXS) after stretching and shape recovery together with simulations of plasmon coupling among the Au NPs provide an understanding of the observed behavior. Controlled clustering of NPs in SMP films and the resulting polarization-dependent optical properties suggest that such clusters of NPs can be useful more broadly for transducing macroscale deformation into locally altered properties. An overview of the methods, mechanism of optical property changes, and application as optical thermal history sensors is presented in Scheme 1.

Scheme 1. Overview of the Methods, Mechanism of Optical Property Changes, and Application of Au NPs Dispersed in Diaplex

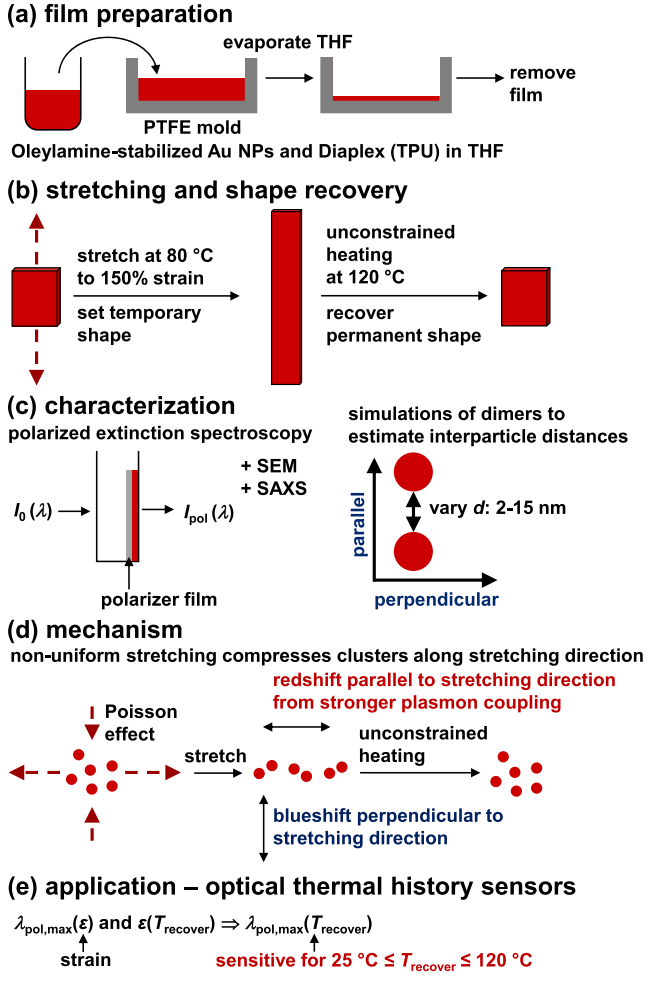

EXPERIMENTAL SECTION

Synthesis and Characterization of Gold Nanoparticles. Spherical Au NPs with an average diameter of 15 nm were synthesized according to an established procedure.[57,58] Chemicals used for synthesizing Au NPs included $HAuCl_4{\cdot}xH_2O$ (Alfa Aesar, 99.999%, where x was estimated as 3), oleylamine (OA, Sigma Aldrich, ≥98% primary amine), anhydrous toluene (EMD, DriSolv), tetrahydrofuran (THF, EMD, OmniSolv, Non-UV), and methanol (MeOH, Macron, ChromAR). The Au NPs are stabilized by OA and are dispersed in THF after purification.

A solution of 24 mL of toluene and 1.5 mL of OA was heated to 115 °C with stirring in a 100 mL round-bottomed flask that was open to an ambient atmosphere. A solution of 50 mg of $HAuCl_4{\cdot}xH_2O$ dissolved in a mixture of 0.5 mL of toluene and 0.6 mL of OA was added and heated while refluxing at 115 °C for 2 h, yielding a red-purple dispersion. The Au NPs were purified by centrifugation after adding a non-solvent to drive sedimentation. The product was divided into two centrifuge tubes, and 3 mL of methanol was added to each tube and centrifuged at 4500 rpm (IEC Centra MP4, 816 rotor, 2900 g) for 2 min. After decanting the supernatant, the sedimented NPs were redispersed in THF.

Transmission electron microscopy (TEM) was performed using a Thermo Scientific Talos F200X microscope by drop casting purified NPs onto Cu TEM grids with ultrathin amorphous carbon supports. Extinction spectra of solutions and of polymer thin films were acquired using an Ocean Optics CHEMUSB4-VIS−NIR spectrophotometer.

Preparation of Shape-Memory Polymer Composite Films. For this study, 7 thin films (~100 μm thick) of Au NPs embedded in a commercially available thermoplastic polyurethane, Diaplex (SMP Technologies, MM5520), were prepared by solvent casting. For each film, 3 mL of THF was added to 0.2 g of Diaplex pellets, which dissolved over a period of 2 h with stirring. A volume of the purified Au NP stock solution containing 4 mg of Au NPs was added to the polymer solution, and then THF was added until the total volume was 5 mL, followed by stirring for another 30 min. The mixture was poured into rectangular polytetrafluoroethylene molds (Savillex 700−925) with dimensions of 10 cm (l) × 2.5 cm (w) × 2 cm (h). Composite NP-Diaplex thin films were obtained after the solvent evaporated for 6−7 h in a fume hood at room temperature. Each film was annealed before stretching at 120 °C for 30 min to remove any residual THF, resulting in a change from a rubbery to paper-like texture.

Stretching Films and Shape Recovery. The films were stretched using a custom-built stretching jig (photograph in the Supporting Information, Figure S1) for uniaxial stretching. Films with a length of 8 cm and width of 2 cm were cut from the middle of each film, clamped in the jig, and stretched using aluminum grips. The middle 2 cm segment of each film was marked with a pen. Each film was placed with 3 cm from each end within the clamps used to pull both ends of the film, giving an active initial length for stretching of 2 cm. The film was stretched until the width of the marked region increased to 5 cm, corresponding to a strain ($\Delta l/l_0$) of 150%. Duplicate sets of three identical films were prepared: (i) before stretching, (ii) stretched, and (iii) after shape recovery. Photographs of the films are shown in the Supporting Information, Figure S2. An additional stretched film was prepared for demonstrating a thermal history sensor.

For stretching, the jig loaded with the film was placed in an oven under ambient atmosphere at 80 °C. Before beginning stretching, the jig was left in the oven for 10 min to thermally equilibrate and soften the film. Stretching was performed in increments of 1 cm by manually rotating a wheel in the jig that pulls the clamps apart, which required briefly opening the door of the oven. Between increments of stretching, the film was left in the oven for intervals of 2 min to maintain the temperature. When markers on the film reached a separation of 5 cm, the film was heated in the oven for another 6 min before removing it for cooling to room temperature. After cooling, the film retained a stretched temporary shape until shape recovery was driven by heating. An oven was used in this study to ensure uniform and complete shape recovery, although the Au NPs in the films can be used to drive shape recovery through photothermal heating.[35] Shape recovery was driven by placing the films unclamped in the oven at 120 °C for 5 min.

Characterization. Optical extinction spectroscopy measurements from one set of the samples were acquired by cutting a rectangular section from the middle of each film with scissors and placing the section in a glass cuvette with the film resting against one wall of the cuvette with the stretching direction oriented vertically. For polarized optical extinction spectroscopy measurements, polarizer films (Edmund Optics 43−781) were cut and placed in the cuvette next to the sample, such that light first went through the polarizer and then through the sample. The designations parallel and perpendicular indicate the relative orientation of the polarization axis with respect to the direction in which the film had been stretched. For polarized measurements, the reference was the polarizer in the corresponding orientation and no sample. All assignments of the wavelengths for the peak maxima were obtained from smoothed spectra (Origin 2020 software, Savitzky−Golay, 201 points, 2nd order polynomial) to remove artifacts caused by noise. For demonstrating an optical thermal history sensor, unconstrained shape recovery was performed on a stretched film that had been cut to a length of 3 cm for placement in the cuvette after heating in a stepwise manner, at 45 °C for 5 min, then 50 °C for 5 min, and heated in increments of 10 °C for 5 min until the final step at 120 °C for 5 min that gave complete shape recovery.

The second set of samples was used for SAXS and SEM. SAXS was performed on a Xeuss 2.0 laboratory beamline by Xenocs (Grenoble, France), which is equipped with a Kα X-ray source (λ = 0.154 nm) and a PILATUS 1 M hybrid photon counting 2D detector from Dectris (Baden, Switzerland). The sample-to-detector distance was set to 2500 mm (calibrated by measuring silver behenate), and the sample was carefully aligned with the stretching direction parallel to the vertical detector axis. Since scattering of the stretched sample was strongly anisotropic, all 2D detector images were transferred into 1D scattering curves by averaging data radially within two different sectors subtending 10° angles either parallel or perpendicular to the stretching direction. For environmental SEM, the samples were placed directly onto the stage of a FEI Quanta 400 FEG ESEM, fixed by a metal ring, and investigated in low-vacuum mode with 100 Pa partial pressure of water added to the chamber and 10 kV accelerating voltage. Secondary and backscattered electrons were collected simultaneously using the ETD and SSD detectors.

Optical Property Simulations. Simulations of the extinction cross section of dimers of Au NPs embedded in a Diaplex matrix film with their interparticle axis within the plane of film were performed using methods described in the Supporting Information. The effects of varying the interparticle distance on the polarized and the unpolarized extinction cross sections were simulated and compared with the experimental results.

RESULTS AND DISCUSSION

The experimental results can be understood by considering the mechanical effects of stretching on the organization of the Au NPs, which have a diameter of 14.5 ± 2.2 nm, measured by TEM (Figure 1). In the as-prepared samples, the Au NPs disperse in Diaplex in small clusters, which is likely caused by interactions between the oleylamine ligands and Diaplex. Dispersing NPs within polymers is a general challenge,[59,60] and it is not surprising that the Au NPs form clusters[61] within the as-prepared Diaplex films. Diaplex is a block copolymer, composed of hard segments that crystallize, methylene diphenyl diisocyanate, soft segments that have a glass transition temperature of ~55 °C, and a chain extender, 1,4-butanediol.[62] The morphology of Diaplex and related thermoplastic polyurethanes when strained is complex and has also been investigated.[63] Prior to stretching, the SPRs of Au NPs within

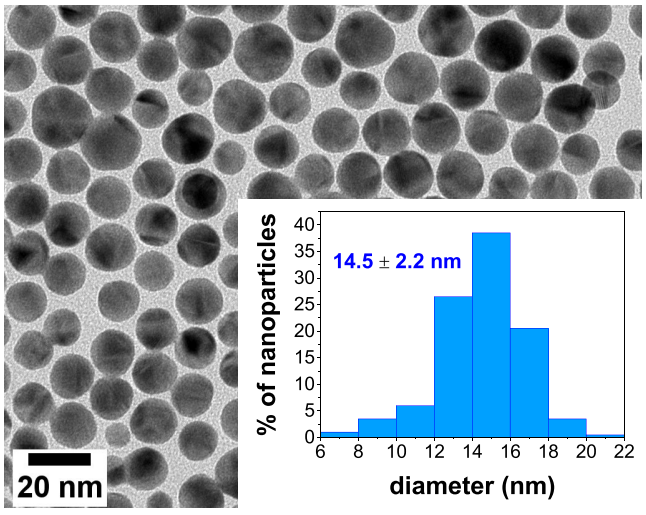

Figure 1. Transmission electron micrograph of Au NPs dropcast from THF with inset histogram of diameter measurements.

the clusters are already coupled, confirmed by the optical properties and structural characterization in the following sections. The optical extinction spectrum undergoes redshifts and blueshifts for light polarized parallel and perpendicular to the stretching direction, respectively. These shifts are consistent with reduced distances between Au NPs within clusters parallel to the stretching direction. Unconstrained heating drives complete shape recovery, and the polarization dependence of the optical extinction vanishes.

Optical Characterization. Au NPs disperse in THF and have maximum extinction at 521 nm (Figure 2a). After dispersion in the polymer film, a redshift in the maximum extinction to 536 nm is observed (Figure 2b). Prior to stretching, the extinction is the same for both polarization directions. In comparison with the experimental results, simulated extinction spectra of isolated Au NPs exhibit maxima at 520 nm in THF and 533 nm in Diaplex (Supporting Information, Figure S3), where the difference arises solely from the different refractive indices of THF and Diaplex. Therefore, theory predicts a shift of 13 nm due to the change in refractive index, while a shift of 15 nm was observed in experiments when dispersing the Au NPs in Diaplex. The additional shift in experiments can be attributed to clustering of the NPs, which was not accounted for in this simulation. The SPR peak also broadens when the Au NPs are dispersed in Diaplex, which we attribute to disorder in the clustering that causes some Au NPs to experience stronger plasmon coupling with their neighbors than others. For quantifying the breadth of the peak, measurements of the full width at three quarters of the maximum (FWTQM) are reported. The FWTQM was chosen instead of the common measurement of the width at half the height to avoid artifacts from the interband transition in Au that is responsible for the broad shoulder in the extinction at shorter wavelengths. The experimental FWTQM for the Au NPs dispersed in THF and embedded within the Diaplex film (unpolarized) is 50 and 60 nm, respectively. Clustering of the Au NPs during preparation of the Diaplex films, resulting in plasmon coupling despite the low loading of the Au NPs in the films, is further confirmed by SEM and SAXS.

For the stretched sample, redshifts and blueshifts were observed for light polarized parallel and perpendicular to the stretching direction, respectively (Figure 2c). We note that

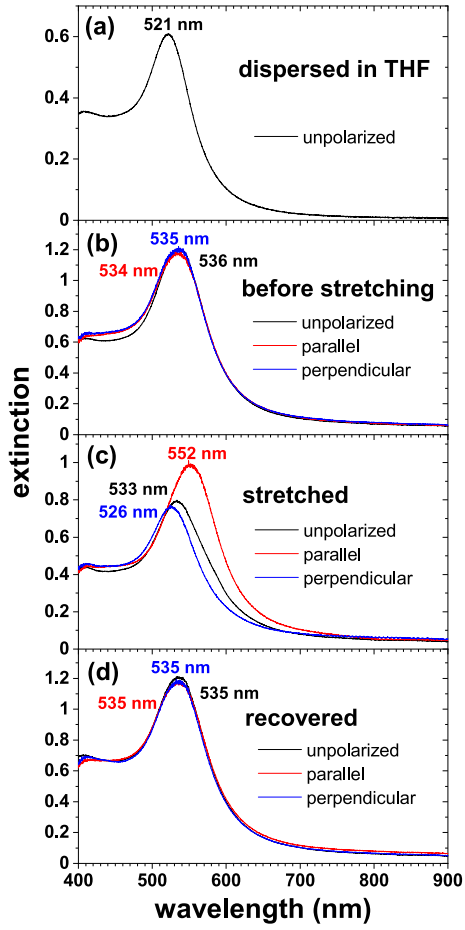

Figure 2. Unpolarized and polarized and optical extinction spectra of Au NPs (a) dispersed in THF and in a Diaplex film (b) before stretching, (c) after stretching at 80 °C, and (d) after heating at 120 °C under zero stress to drive shape recovery.

there is an error in measuring the wavelength of the maximum extinction, which is reasonable given the inexpensive spectrophotometer and polarizer films. The data presented were not smoothed, but smoothing was performed to reduce noise from random error for identifying the maxima. As an example for estimating the error remaining after smoothing, the peaks in Figure 2b should all have the same wavelength, and the maxima are assigned in a narrow window of 534−536 nm. Control experiments of all samples between crossed polarizers confirmed negligible or zero birefringence in any of the polymer films (Supporting Information, Figure S4). After heating under zero stress to drive shape recovery, the blue- and redshifts vanished (Figure 2d). The sample exhibits complete macroscale and nanoscale shape recovery to its initial shape, which is also confirmed by structural characterization. The wavelengths at the extinction maxima are summarized in Table 1. Despite significant shifts in their polarized extinction spectra after stretching, the peaks of unpolarized extinction spectra for the films lie within a narrow window of 533−536 nm.

Scanning Electron Microscopy. SEM images show variability within the films before stretching. Some regions have a higher density of larger clusters of Au NPs, and other regions have more disperse, smaller clusters, dimers, and individual Au NPs (Figure 3a). Since most of the Au NPs are present in clusters, plasmon coupling is expected, as already anticipated from the extinction spectra. Moreover, the

Table 1. Measurements of Peak Wavelength and Breadth in Unpolarized (UNP) and Polarized (⊥ and ∥) Optical Extinction Spectra for all Samples

figure	sample	1. ∥ (nm)	2. ⊥ (nm)	3. UNP (nm)	FWTQM[a] (nm)	Δ(1−3) (nm)	Δ(3−2) (nm)	Sep[b] (nm)
2a	in THF			521	50			
2b	before stretching	534	535	536	60	−2	1	>6[d]
2c	stretched	552	526	533	60	19	7	4[c]
2d	recovered	535	535	535	62	0	0	>6[d]

[a]FWTQM was measured from unpolarized spectra. [b]Average interparticle separation (Sep) between the metal surfaces of Au NPs based on comparison with simulations of dimers of Au NPs. [c]From comparison with simulated polarized optical extinction spectra (Figure 5) for the stretched sample. [d]From comparison with unpolarized optical extinction spectra (Supporting Information, Figure S6) for unstretched samples that did not exhibit polarization effects. At wavelengths below ∼540 nm, corresponding to interparticle separations exceeding 6 nm, the sensitivity of the peak wavelength to the interparticle separation distance is diminished.

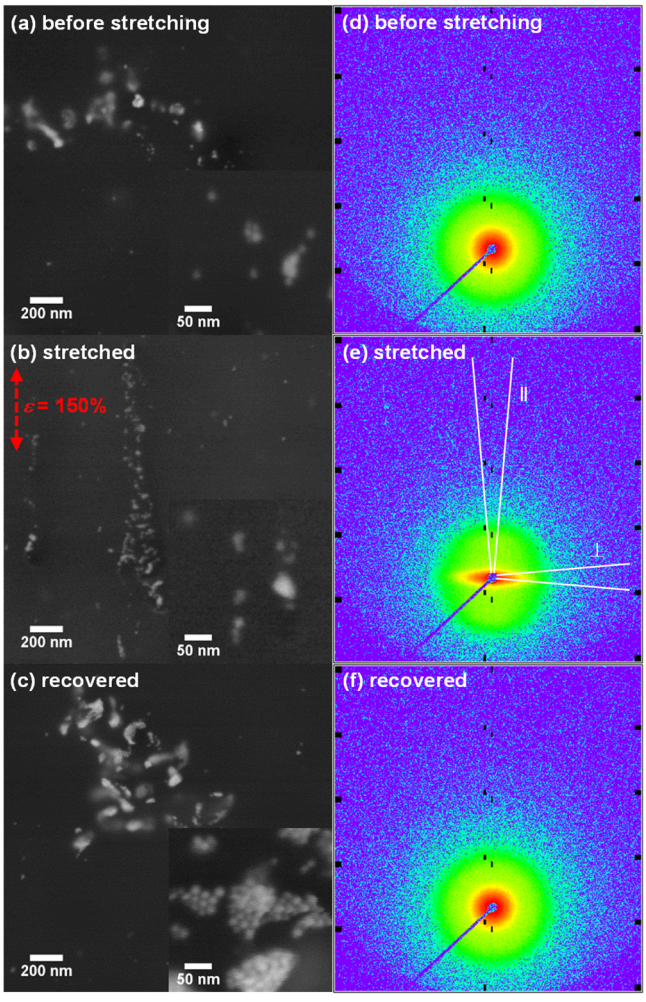

Figure 3. SEM images from backscattered electrons and 2D detector images of SAXS measurements for samples loaded with Au NPs (a, d) before stretching, (b, e) stretched, and (c, f) after shape recovery. SAXS detector images have a logarithmic color scale from red (high intensity) to purple (low intensity), and two different sectors parallel and perpendicular to the stretching direction are shown for the stretched sample. The black spots are due to intermodular detector gaps.

distribution of arrangements would be expected to cause differences in plasmon coupling among Au NPs, which is reflected in the increase in the FWTQM when the Au NPs are dispersed in the Diaplex film. In the stretched sample, more of the clusters appear to be aligned parallel to the stretching direction, which is consistent with shearing during stretching (Figure 3b). After shape recovery, the same isotropic configuration is observed as before stretching, and there is no evidence of stretching (Figure 3c). Because SEM images provide information about only a small region of the sample, it is challenging to obtain images that are quantitatively representative of the microstructure of the sample from SEM. Furthermore, the spatial resolution in SEM of the arrangements of plasmon-coupled Au NPs embedded in the polymer is rather limited. SAXS measurements and optical property simulations provide a more detailed understanding. It is also important to note that information from two-dimensional SEM images about the arrangement of the NPs in the out-of-plane direction is limited.

Small Angle X-Ray Scattering. A first impression of the SAXS results is given by the 2D detector images of the films loaded with Au NPs (Figure 3d−f). Before stretching and after shape recovery, scattering is isotropic. The detector image for the stretched sample becomes highly anisotropic, however, with respective increases and decreases in the intensity for small scattering angles in the perpendicular and parallel directions. Because of the anisotropy of the stretched sample, scattering measurements for the parallel and perpendicular directions of all three samples are analyzed. In 1D scattering curves (Figure 4), scattering is dominated by the Au NPs. The contrast of the polymer is too weak to resolve in the presence of Au NPs. For large scattering vectors q, corresponding to short length scales, all curves overlap and have similar features. Scattering in this high-q regime is dominated by single Au NPs that are identical in all three samples and do not reshape during the stretching and recovery processes. In Figure 4b, an exemplary fit to the high-q regime with a spherical form-factor model is shown for the stretched sample. The resulting NP diameter from this fit is 13.4 ± 2.7 nm, which agrees well with the size distribution from TEM measurements. Among all six measurements (three samples and two scattering directions), the diameter from fitting is in the range of 13.2−13.4 nm, essentially the same value.

At smaller q corresponding to length scales larger than size of the Au NPs, scattering gives information on correlations between NPs, which cannot be described by a pure form-factor model. In nanocomposites, these correlations typically encapsulate a broader distribution of separations between NPs and different sizes of agglomerates; thus, SAXS patterns do not show distinct peaks but instead have different power laws. The value of q at which one power-law behavior turns into another one, a change of slopes in the log−log representation is observed and can then be associated with a characteristic length scale.[64] Due to the broad distribution of separations and sizes, these q values are difficult to determine

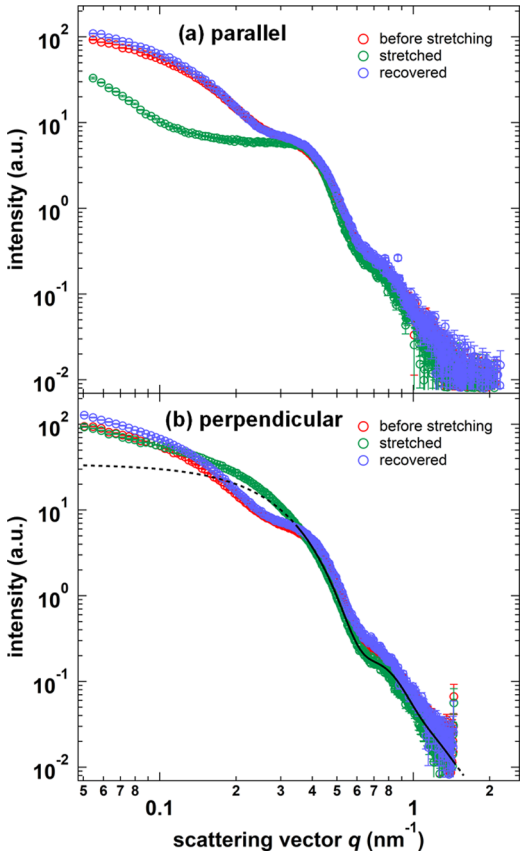

Figure 4. 1D scattering curves from SAXS measurements for samples loaded with Au NPs evaluated (a) parallel and (b) perpendicular to the stretching direction. The solid black line in (b) is an exemplary fit of a polydisperse spherical form-factor model to the scattering curve of the stretched sample, which is extrapolated as the dashed line.

in the 1D scattering curves but become much more prominent in Kratky plots, where the scattered intensity is multiplied by q^2 (Supporting Information, Figure S5). In this representation, slope changes are transformed into peaks, and the peaks in q can be assigned with high reliability by fitting to log-normal distributions. Before stretching and in the recovered sample, the Kratky plot reveals two peaks that can be attributed to the size of the agglomerates ($q \approx 0.15$ nm^{-1}) and the center-to-center NP distance ($q \approx 0.4$ nm^{-1}). During stretching, these two peaks are affected rather differently for the parallel and perpendicular directions. Parallel to the stretching direction, the interparticle peak remains unchanged, while the peak for the agglomerates vanishes, presumably by shifting to much smaller q that cannot be observed with our SAXS instrument. In contrast, in the perpendicular direction, only one broad feature is observed, which is decomposed by fitting a sum of two log-normal distributions (dashed lines in the Supporting Information, Figure S5b) to an almost unchanged peak for the agglomerate size and an interparticle peak shifted to smaller q values. From the log-normal distribution of the peak associated with agglomerates, the average agglomerate size $2\pi/q^*$ is 29 ± 20 nm for all samples except for the stretched parallel case. This calculation uses q^*, the median value that occurs at a q slightly larger than the maximum because of the asymmetry of the log-normal distribution.[64] If the absence of the peak for the agglomerate size is indeed caused by its shift to lower q, then a minimum agglomerate size of 125 nm can be estimated from the lowest measured q of 0.05 nm^{-1}. Indeed, the most obvious effect of stretching observed by SAXS is the anisotropy at low q that is diminished at higher q (Figure 3e). Stretching dramatically increases the size of the agglomerates parallel to the stretching direction, which is consistent with linear aggregates observed by SEM (Figure 3b).

The interparticle distances are expected to correlate with the optical properties, since plasmon coupling strongly depends on the separation distance, which we discuss as a function of surface-to-surface distances. The position of the interparticle peak observed by SAXS is directly related to the center-to-center distance of the NPs, from which the surface−surface distance can be obtained by subtracting the diameter of the NPs. Due to the rather broad distributions of diameters ($\sigma \approx$ 20%) and center-to-center distances ($\sigma \approx$ 22−39%) obtained from analysis of the SAXS measurements, it is not possible to reliably determine the surface−surface distances from SAXS. This outcome is not surprising given the significant heterogeneity shown by SEM. We therefore discuss only the measured center-to-center distances, which would nevertheless indicate how the surface-to-surface distance for the different samples may change. In the parallel direction, the Kratky plots show minimal influence of stretching on the position of the interparticle peak. The center−center distances remain nearly constant at 16 ± 4 nm before stretching and after shape recovery, with a minor compression of ∼0.5 nm caused by stretching. The same center−center distances are measured perpendicular to the stretching direction for samples before stretching and after shape recovery, as would also be expected based on their isotropy. Therefore, the most significant change of interparticle distances noted by SAXS is for the stretched sample in the perpendicular direction, which has a significant increase in center-to-center distances and a broadening of their distribution (20 ± 8 nm). Thus, SAXS results for center-to-center distances are consistent with the optical measurements of a blueshift of the SPR peak in the perpendicular direction. A decrease of the center-to-center distance in the parallel direction corresponding to the redshifted SPR peak is barely discernible by SAXS, which we attribute to the large errors in the center-to-center distances.

Optical Property Simulations. Simulations further support interpretation of the polarized extinction spectra and establish a relationship between the redshift in the SPR and the average interparticle spacing, demonstrating an approach for applying plasmon ruler concepts in plasmonic polymer composites. Shifts in the SPR peak measured in polarized extinction spectra indicate that during stretching, the distance between Au NPs within clusters decreases along the stretching direction. In addition to SEM and SAXS, which both provide limited quantification of interparticle distances due to limited resolution and disorder in the sample, respectively, we report simulations to support our interpretation of the polarized optical properties and to estimate the interparticle distances between the Au NPs whose plasmons are coupled.

Simulations are consistent with experiments and the above explanation, where stretching increases coupling of Au NPs along the stretching direction. Dimers of Au NPs were selected for modeling for their simplicity and because many of the experimentally observed clusters are small. Dimers are a logical choice because this avoids having to otherwise choose an arbitrary number of NPs in a cluster and an arbitrary arrangement for the cluster. In many instances even for larger clusters of Au NPs, the shifts in the SPR plasmon peak may also be dominated by pairwise interactions consistent with

dimers because of the structural heterogeneity within the clusters observed by SEM (Figure 3). The simulated dimers were oriented within the plane of the film because the shear forces of stretching would be expected to align them with the stretching direction.

The main comparison between experimental and simulated optical extinction spectra is the wavelength of the SPR maximum. The comparison is limited in some instances by the breadth of the experimental SPR spectral peaks, as opposed to the narrow, simulated spectral peaks. For the stretched sample, interparticle separation distances can be chosen for the simulated dimers that produce polarized SPR maxima in good agreement with those of the experiments for both polarization directions simultaneously (Figure 5). Simulations

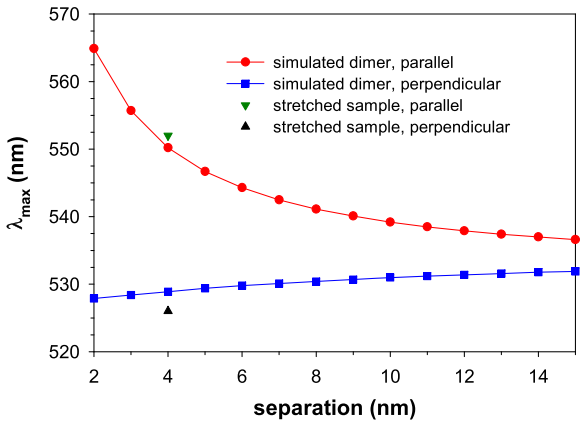

Figure 5. Maximum wavelength from polarized optical extinction spectra vs interparticle surface-to-surface separation for dimers of Au NPs from simulations with experimental data points for maximum wavelengths for the stretched sample added to match the simulations, thereby estimating the average interparticle distances. For simulations and the experimental sample, parallel and perpendicular indicate the polarization direction with respect to the interparticle axis and the stretch direction, respectively.

of the dimer parallel to its axis of interparticle separation are compared with experiments parallel to the stretching direction, along which the Au NPs are pulled closer together, which are both redshifted due to the strong plasmon coupling.

The redshift for polarization parallel to the axis of interparticle separation is significantly stronger than the blueshift for polarization perpendicular to the same axis. The interparticle separation distance, which is used as a parameter for matching the experimental and simulated results, is extracted from the analysis. An interparticle separation distance of 4 nm is estimated along the stretching direction in the stretched sample. This distance might be somewhat shorter than the actual average interparticle distances, where extended plasmon coupling in plasmonic oligomers[65−67] is not accounted for and would instead be encapsulated in a reduction in the interparticle distance of a dimer.

While the parallel polarization is of greatest interest in this work because of its strong sensitivity, there is further subtlety in understanding the cause of the blueshift in the perpendicular direction. We have already shown that stretching decreases the interparticle distances along the stretching direction, which is accompanied by an increase in the interparticle distance perpendicular to the stretching direction, as confirmed by SAXS measurements. The increased distances in the perpendicular direction would be expected to cause a blueshift for the perpendicular polarization, but this does not sufficiently explain the experimental observations: The simulated peak extinction for uncoupled Au NPs dispersed in Diaplex occurs at 533 nm (Supporting Information, Figure S3). Therefore, increasing the separation of Au NPs should not produce a blueshift beyond 533 nm, but 526 nm was observed for the stretched sample, perpendicular polarization. Rather, the stronger plasmon coupling from decreased interparticle spacing in the stretching direction intrinsically causes both a redshift parallel to and a blueshift perpendicular to the stretching direction, which is well represented in the simulations of the dimers (Figure 5 and Supporting Information, Figure S7). This property of plasmon coupling is the predominant effect responsible for the blueshift for perpendicular polarization.

In addition to plasmon coupling, another complex phenomenon that should be considered for potentially causing shifts in the SPR extinction wavelength is changes in the polymer microstructure and dielectric environment caused by stretching, especially in a multiphase polymer. Such an effect could be of interest for future investigation and purposeful control of the SPR but is neglected here. Based on the chemical functionalization of the Au NPs, they are more likely to disperse in one phase within the Diaplex block copolymer, which would tend to reduce the magnitude of the dielectric effect. Furthermore, if dielectric inhomogeneities within the environment would have a substantial effect on the optical properties, much more dramatic broadening of the SPR peak would be expected than we have observed. The significant inhomogeneities in the distribution of Au NPs within the clusters would further be expected to cause large variations of the shift in the SPR. Therefore, we believe that the prevailing effect controlling the changes in the optical properties is plasmon coupling.

As a further test of the method for comparing the maxima of experimental and simulated optical extinction spectra to estimate the interparticle separation distance, we also compared the unpolarized spectra for the stretched sample (Supporting Information, Figure S6). The spectra from unpolarized light incident perpendicular to the film should be independent of the angle of the dimer within the plane of the film, with equal weighting of the two orthogonal polarization components that comprise unpolarized light. As such, we simulated the unpolarized extinction spectra for a single dimer by computing the average of the two extinction cross sections obtained with light polarized either parallel or perpendicular to the dimer axis (Supporting Information, Figure S7).

The unpolarized spectrum and the wavelength of its maximum are dominated by the parallel polarization direction. The interparticle separations already established from the polarized optical extinction spectra for the stretched sample do not yield a good match with the unpolarized spectra (Supporting Information, Figure S6). This apparent lack of self-consistency can be attributed to the significantly greater width of the experimental peaks than the simulated peaks. Specifically, for short interparticle separation distances below ~5 nm, averaging the extinction cross sections of the parallel and perpendicular polarizations to obtain the unpolarized spectrum yields a redshifted spectrum with a significant shoulder on the blue side of the peak (Supporting Information, Figure S7c). If the peaks for each polarization would be

broader, as they are in the experimental spectra, then the maximum wavelength of the unpolarized SPR peak would be blueshifted. Therefore, the shortcoming of comparing the unpolarized extinction spectra at short interparticle separation distances is the dependence on the width of the peaks, which is mismatched between experiments and simulations. The Au NPs in the experimental samples have many different arrangements, with some having their SPRs more strongly coupled than others, which causes broadening in the extinction spectrum. To highlight that the experimental peaks are much broader, the experimental and simulated polarized optical extinction spectra for the stretched sample are plotted in the Supporting Information, Figure S8.

Optical Thermal History Sensor. When optimizing the conditions for obtaining complete shape recovery, we found that using a sufficiently high temperature for shape recovery is important for achieving complete recovery of the permanent shape and the return to its initial optical properties (Figure 6). The temperature dependence of the polarized extinction spectra can be applied for thermal history sensing,[68] where shifts in the parallel polarization are larger and therefore offer greater sensitivity than the perpendicular polarization direction. Recovery at temperatures below 120 °C is incomplete, and the temperature to which the sample was exposed correlates with the peak wavelength of the polarized extinction spectrum (Figure 6d) and the strain obtained from measuring the length of the sample (Figure 6e). Therefore, this material provides an optical readout of the thermal history. The peak wavelengths for both polarization directions and strain have an approximately linear dependence on the recovery temperature, but we are not aware of a fundamental reason to anticipate such a trend, given the complex relationships between macroscale strain, non-uniform rearrangements of Au NPs during stretching, plasmon coupling, and the kinetics of thermal shape recovery of shape-memory polymers.

The extinction peak intensity also increases monotonically during the recovery process because of the Poisson effect. Contraction of the film during shape recovery increases the thickness of the film, bringing more Au NPs into the optical beam path. The extinction peak intensity is less reliable for this sensing application, however, because variations in the film thickness provide more noise. Furthermore, extinction is an extensive quantity and is also affected by the strength of plasmon coupling, while the wavelength is an intensive property that does not depend on the thickness of the film. It should also be noted that the sample prior to recovery (corresponding to a recovery temperature of 25 °C, room temperature) had a measured strain of 140%, while 150% was expected. The difference is due to minor slippage in the grips of the stretching jig.

The transition temperature of the SMP matrix is expected to determine the range of the thermal sensitivity for the film, which could allow designs for sensing over different temperatures ranges. It should also be noted that annealing the permanent shape prior to stretching is also important for removing residual solvent and providing consistent performance, which converts the texture of the films from rubber-like to paper-like. While thermal history sensors are generally designed for single use, this material could potentially be used multiple times, if manually heated and restretched between cycles.

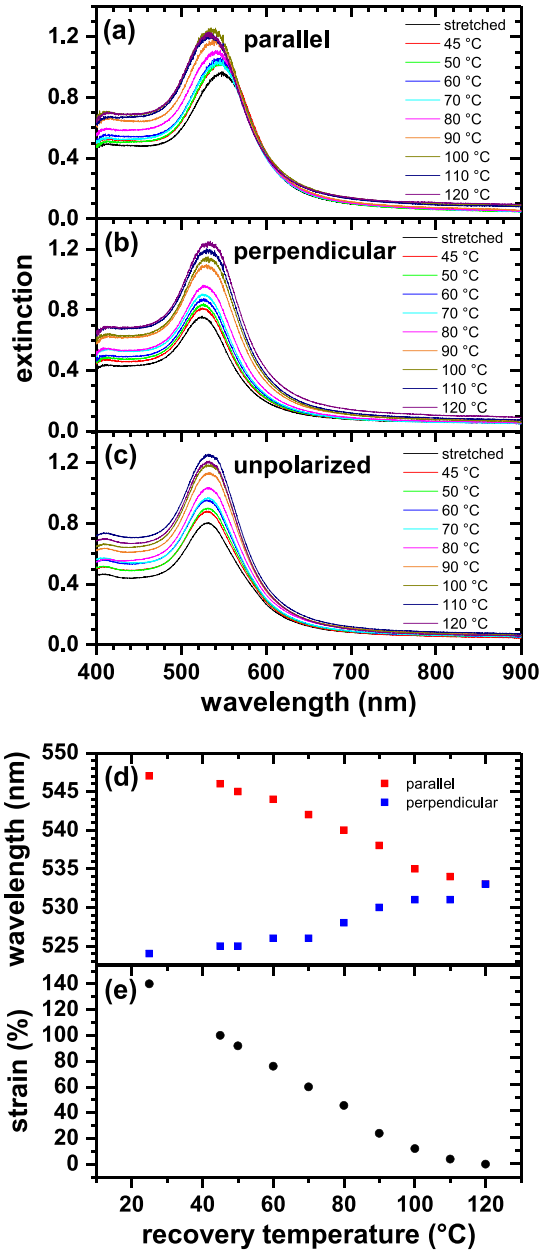

Figure 6. Optical extinction spectra for stretched Diaplex films with embedded Au NPs and after stepwise shape recovery under zero applied stress during heating from 45 to 120 °C with hold times of 5 min at each step for polarization (a) parallel and (b) perpendicular to the stretching direction or (c) unpolarized. (d) Wavelength of the maximum of the extinction peak for both polarization directions and (e) strain measured from the length of the active region of the film during the heating steps to drive shape recovery.

CONCLUSIONS

In this work, formation of clusters of Au NPs during preparation of SMP nanocomposites causes coupling of their plasmons. Stretching these films results in significantly altered optical properties because the average interparticle spacing decreases along the stretching direction. Use of an SMP for the polymeric matrix allows setting a temporary shape with a significant polarization-dependent optical response, followed by complete macroscale and nanoscale shape recovery. Structural characterization and simulations of the optical properties provide insights about the structural changes that

occur during stretching and shape recovery. The dependence of plasmon coupling among the Au NPs on the strain during shape recovery, which depends on the recovery temperature, makes these materials useful as optical thermal history sensors.

We note that this study used a low loading of Au NPs to maintain optically transmissive films. Future work could include further investigating the effects of the loading and processing conditions on the clustering behavior of the Au NPs. Furthermore, patterning the NPs could make possible programming of the optical property changes that occur during stretching and shape recovery. Specifically, use of advanced self-assembly techniques, potentially including microfabricated templates, could control the formation of clusters of NPs, which may be extended beyond Au. Simulations of both the mechanical response of the polymer and the optical response of the NP assembly would allow for the predictive design of responsive and reconfigurable plasmonic nanocomposites. In addition to optically detecting the thermal history, more advanced future materials may have programmable mechanical and thermal modulation of the optical properties.

■ ASSOCIATED CONTENT

Supporting Information

The Supporting Information is available free of charge at https://pubs.acs.org/doi/10.1021/acsanm.1c00309.

Details for optical property simulations, photographs of stretching jig and films, optical extinction measurements with crossed polarizers, analysis of SAXS measurements, polarized and unpolarized simulated optical extinction spectra, and analysis of unpolarized experimental and simulated optical extinction spectra (PDF)

Polarization effects of stretched sample (Video S1) (MPG)

■ AUTHOR INFORMATION

Corresponding Author

Joseph B. Tracy − *Department of Materials Science and Engineering, North Carolina State University, Raleigh, North Carolina 27695, United States;* orcid.org/0000-0002-3358-3703; Email: jbtracy@ncsu.edu

Authors

Prachi R. Yadav − *Department of Materials Science and Engineering, North Carolina State University, Raleigh, North Carolina 27695, United States*

Mehedi H. Rizvi − *Department of Materials Science and Engineering, North Carolina State University, Raleigh, North Carolina 27695, United States*

Björn Kuttich − *INM - Leibniz Institute for New Materials, 66123 Saarbrüken, Germany;* orcid.org/0000-0002-5380-581X

Sumeet R. Mishra − *Department of Materials Science and Engineering, North Carolina State University, Raleigh, North Carolina 27695, United States*

Brian S. Chapman − *Department of Materials Science and Engineering, North Carolina State University, Raleigh, North Carolina 27695, United States*

Brian B. Lynch − *Department of Materials Science and Engineering, North Carolina State University, Raleigh, North Carolina 27695, United States;* orcid.org/0000-0002-4407-4541

Tobias Kraus − *INM - Leibniz Institute for New Materials, 66123 Saarbrüken, Germany; Colloid and Interface Chemistry, Saarland University, 66123 Saarbrüken, Germany;* orcid.org/0000-0003-2951-1704

Amy L. Oldenburg − *Department of Physics & Astronomy, University of North Carolina, Chapel Hill, North Carolina 27599, United States*

Complete contact information is available at: https://pubs.acs.org/10.1021/acsanm.1c00309

Notes

The authors declare no competing financial interest.

■ ACKNOWLEDGMENTS

This research was supported by the National Science Foundation (CMMI-1663416, CBET-1803830, and CBET-1803785), National Institutes of Health (R21 HL 130901), and the Alexander von Humboldt Foundation. We thank Marcus Koch, Charles Mooney, Phillip Strader, and Neal Lewis for assistance with scanning electron microscopy, Jessica Liu for assistance with video editing, and Tobias König for helpful discussions. This work was performed in part at the Analytical Instrumentation Facility (AIF) at North Carolina State University, which is supported by the State of North Carolina and the National Science Foundation (ECCS-1542015). The AIF is a member of the Research Triangle Nanotechnology Network (RTNN), a site in the National Nanotechnology Coordinated Infrastructure (NNCI).

■ REFERENCES

(1) Bockstaller, M. R.; Lapetnikov, Y.; Margel, S.; Thomas, E. L. Size-Selective Organization of Enthalpic Compatibilized Nanocrystals in Ternary Block Copolymer/Particle Mixtures. *J. Am. Chem. Soc.* **2003**, *125*, 5276−5277.

(2) Böker, A.; Lin, Y.; Chiapperini, K.; Horowitz, R.; Thompson, M.; Carreon, V.; Xu, T.; Abetz, C.; Skaff, H.; Dinsmore, A. D.; Emrick, T.; Russell, T. P. Hierarchical Nanoparticle Assemblies Formed by Decorating Breath Figures. *Nat. Mater.* **2004**, *3*, 302−306.

(3) Bockstaller, M. R.; Mickiewicz, R. A.; Thomas, E. L. Block Copolymer Nanocomposites: Perspectives for Tailored Functional Materials. *Adv. Mater.* **2005**, *17*, 1331−1349.

(4) Balazs, A. C.; Emrick, T.; Russell, T. P. Nanoparticle Polymer Composites: Where Two Small Worlds Meet. *Science* **2006**, *314*, 1107−1110.

(5) Winey, K. I.; Vaia, R. A. Polymer Nanocomposites. *MRS Bull.* **2007**, *32*, 314−322.

(6) Vaia, R. A.; Maguire, J. F. Polymer Nanocomposites with Prescribed Morphology: Going beyond Nanoparticle-Filled Polymers. *Chem. Mater.* **2007**, *19*, 2736−2751.

(7) Choi, J. H.; Adams, S. M.; Ragan, R. Design of a Versatile Chemical Assembly Method for Patterning Colloidal Nanoparticles. *Nanotechnology* **2009**, *20*, No. 065301.

(8) Zheng, X.; Fontana, J.; Pevnyi, M.; Ignatenko, M.; Wang, S.; Vaia, R.; Palffy-Muhoray, P. The Effects of Nanoparticle Shape and Orientation on the Low Frequency Dielectric Properties of Nanocomposites. *J. Mater. Sci.* **2012**, *47*, 4914−4920.

(9) Jang, S. G.; Audus, D. J.; Klinger, D.; Krogstad, D. V.; Kim, B. J.; Cameron, A.; Kim, S.-W.; Delaney, K. T.; Hur, S.-M.; Killops, K. L.; Fredrickson, G. H.; Kramer, E. J.; Hawker, C. J. Striped, Ellipsoidal Particles by Controlled Assembly of Diblock Copolymers. *J. Am. Chem. Soc.* **2013**, *135*, 6649−6657.

(10) Kao, J.; Xu, T. Nanoparticle Assemblies in Supramolecular Nanocomposite Thin Films: Concentration Dependence. *J. Am. Chem. Soc.* **2015**, *137*, 6356−6365.

(11) Liz-Marzán, L. M. Tailoring Surface Plasmons through the Morphology and Assembly of Metal Nanoparticles. *Langmuir* **2006**, *22*, 32−41.
(12) Li, Q.; He, J.; Glogowski, E.; Li, X.; Wang, J.; Emrick, T.; Russell, T. P. Responsive Assemblies: Gold Nanoparticles with Mixed Ligands in Microphase Separated Block Copolymers. *Adv. Mater.* **2008**, *20*, 1462−1466.
(13) Sannomiya, T.; Hafner, C.; Vörös, J. Strain Mapping with Optically Coupled Plasmonic Particles Embedded in a Flexible Substrate. *Opt. Lett.* **2009**, *34*, 2009−2011.
(14) Nepal, D.; Onses, M. S.; Park, K.; Jespersen, M.; Thode, C. J.; Nealey, P. F.; Vaia, R. A. Control over Position, Orientation, and Spacing of Arrays of Gold Nanorods Using Chemically Nanopatterned Surfaces and Tailored Particle−Particle−Surface Interactions. *ACS Nano* **2012**, *6*, 5693−5701.
(15) Kan, T.; Matsumoto, K.; Shimoyama, I. Optical Measurement of Directional Strain by Scattering from Nano-Disk Pairs Aligned on an Elastomer. *Nanotechnology* **2012**, *23*, 315201.
(16) Kim, Y.; Zhu, J.; Yeom, B.; Di Prima, M.; Su, X.; Kim, J.-G.; Yoo, S. J.; Uher, C.; Kotov, N. A. Stretchable Nanoparticle Conductors with Self-Organized Conductive Pathways. *Nature* **2013**, *500*, 59−63.
(17) Gupta, M. K.; König, T.; Near, R.; Nepal, D.; Drummy, L. F.; Biswas, S.; Naik, S.; Vaia, R. A.; El-Sayed, M. A.; Tsukruk, V. V. Surface Assembly and Plasmonic Properties in Strongly Coupled Segmented Gold Nanorods. *Small* **2013**, *9*, 2979−2990.
(18) Ferrier, R. C., Jr.; Lee, H.-S.; Hore, M. J. A.; Caporizzo, M.; Eckmann, D. M.; Composto, R. J. Gold Nanorod Linking to Control Plasmonic Properties in Solution and Polymer Nanocomposites. *Langmuir* **2014**, *30*, 1906−1914.
(19) Hanske, C.; Tebbe, M.; Kuttner, C.; Bieber, V.; Tsukruk, V. V.; Chanana, M.; König, T. A. F.; Fery, A. Strongly Coupled Plasmonic Modes on Macroscopic Areas via Template-Assisted Colloidal Self-Assembly. *Nano Lett.* **2014**, *14*, 6863−6871.
(20) Han, X.; Liu, Y.; Yin, Y. Colorimetric Stress Memory Sensor Based on Disassembly of Gold Nanoparticle Chains. *Nano Lett.* **2014**, *14*, 2466−2470.
(21) Kim, Y.; Yeom, B.; Arteaga, O.; Jo Yoo, S.; Lee, S.-G.; Kim, J.-G.; Kotov, N. A. Reconfigurable Chiroptical Nanocomposites with Chirality Transfer from the Macro- to the Nanoscale. *Nat. Mater.* **2016**, *15*, 461−468.
(22) Maldonado, M.; Baltar, H. T. M. C. M.; Gomes, A. S. L.; Vaia, R.; Park, K.; Che, J.; Hsiao, M.; de Araújo, C. B.; Baev, A.; Prasad, P. N. Coupled-Plasmon Induced Optical Nonlinearities in Anisotropic Arrays of Gold Nanorod Clusters Supported in a Polymeric Film. *J. Appl. Phys.* **2017**, *121*, 143103.
(23) Hsu, S.-W.; Rodarte, A. L.; Som, M.; Arya, G.; Tao, A. R. Colloidal Plasmonic Nanocomposites: From Fabrication to Optical Function. *Chem. Rev.* **2018**, *118*, 3100−3120.
(24) Caseri, W. Nanocomposites of Polymers and Metals or Semiconductors: Historical Background and Optical Properties. *Macromol. Rapid Commun.* **2000**, *21*, 705−722.
(25) Zhang, Y.; Liu, Q.; Mundoor, H.; Yuan, Y.; Smalyukh, I. I. Metal Nanoparticle Dispersion, Alignment, and Assembly in Nematic Liquid Crystals for Applications in Switchable Plasmonic Color Filters and E-Polarizers. *ACS Nano* **2015**, *9*, 3097−3108.
(26) Kennedy, W. J.; Slinker, K. A.; Volk, B. L.; Koerner, H.; Godar, T. J.; Ehlert, G. J.; Baur, J. W. High-Resolution Mapping of Thermal History in Polymer Nanocomposites: Gold Nanorods as Microscale Temperature Sensors. *ACS Appl. Mater. Interfaces* **2015**, *7*, 27624−27631.
(27) Caseri, W. R. Dichroic Nanocomposites Based on Polymers and Metallic Particles: From Biology to Materials Science. *Polym. Int.* **2018**, *67*, 46−54.
(28) Homaeigohar, S.; Elbahri, M. Switchable Plasmonic Nanocomposites. *Adv. Opt. Mater.* **2019**, *7*, 1801101.
(29) Qian, X.; Zhao, Y.; Alsaid, Y.; Wang, X.; Hua, M.; Galy, T.; Gopalakrishna, H.; Yang, Y.; Cui, J.; Liu, N.; Marszewski, M.; Pilon, L.; Jiang, H.; He, X. Artificial Phototropism for Omnidirectional Tracking and Harvesting of Light. *Nat. Nanotechnol.* **2019**, *14*, 1048−1055.
(30) Meng, H.; Li, G. A Review of Stimuli-Responsive Shape Memory Polymer Composites. *Polymer* **2013**, *54*, 2199−2221.
(31) Zhao, Q.; Qi, H. J.; Xie, T. Recent Progress in Shape Memory Polymer: New Behavior, Enabling Materials, and Mechanistic Understanding. *Prog. Polym. Sci.* **2015**, *49-50*, 79−120.
(32) Safranski, D. Introduction to Shape-Memory Polymers. In *Shape-Memory Polymer Device Design*; Safranski, D. L.; Griffis, J. C., Eds. William Andrew Publishing: 2017; pp. 1−22.
(33) Liu, J. A.-C.; Gillen, J. H.; Mishra, S. R.; Evans, B. A.; Tracy, J. B. Photothermally and Magnetically Controlled Reconfiguration of Polymer Composites for Soft Robotics. *Sci. Adv.* **2019**, *5*, No. eaaw2897.
(34) Liu, J. A.-C.; Evans, B. A.; Tracy, J. B. Photothermally Reconfigurable Shape Memory Magnetic Cilia. *Adv. Mater. Technol.* **2020**, *5*, 2000147.
(35) Mishra, S. R.; Tracy, J. B. Sequential Actuation of Shape-Memory Polymers through Wavelength-Selective Photothermal Heating of Gold Nanospheres and Nanorods. *ACS Appl. Nano Mater.* **2018**, *1*, 3063−3067.
(36) Sönnichsen, C.; Reinhard, B. M.; Liphardt, J.; Alivisatos, A. P. A Molecular Ruler Based on Plasmon Coupling of Single Gold and Silver Nanoparticles. *Nat. Biotechnol.* **2005**, *23*, 741−745.
(37) Jain, P. K.; Huang, W.; El-Sayed, M. A. On the Universal Scaling Behavior of the Distance Decay of Plasmon Coupling in Metal Nanoparticle Pairs: A Plasmon Ruler Equation. *Nano Lett.* **2007**, *7*, 2080−2088.
(38) Langer, J.; Jimenez de Aberasturi, D.; Aizpurua, J.; Alvarez-Puebla, R. A.; Auguié, B.; Baumberg, J. J.; Bazan, G. C.; Bell, S. E. J.; Boisen, A.; Brolo, A. G.; Choo, J.; Cialla-May, D.; Deckert, V.; Fabris, L.; Faulds, K.; García de Abajo, F. J.; Goodacre, R.; Graham, D.; Haes, A. J.; Haynes, C. L.; Huck, C.; Itoh, T.; Käll, M.; Kneipp, J.; Kotov, N. A.; Kuang, H.; Le Ru, E. C.; Lee, H. K.; Li, J.-F.; Ling, X. Y.; Maier, S. A.; Mayerhöfer, T.; Moskovits, M.; Murakoshi, K.; Nam, J.-M.; Nie, S.; Ozaki, Y.; Pastoriza-Santos, I.; Perez-Juste, J.; Popp, J.; Pucci, A.; Reich, S.; Ren, B.; Schatz, G. C.; Shegai, T.; Schlücker, S.; Tay, L.-L.; Thomas, K. G.; Tian, Z.-Q.; Van Duyne, R. P.; Vo-Dinh, T.; Wang, Y.; Willets, K. A.; Xu, C.; Xu, H.; Xu, Y.; Yamamoto, Y. S.; Zhao, B.; Liz-Marzán, L. M. Present and Future of Surface-Enhanced Raman Scattering. *ACS Nano* **2020**, *14*, 28−117.
(39) Qian, Z.; Ginger, D. S. Reversibly Reconfigurable Colloidal Plasmonic Nanomaterials. *J. Am. Chem. Soc.* **2017**, *139*, 5266−5276.
(40) van der Zande, B. M. I.; Pagès, L.; Hikmet, R. A. M.; van Blaaderen, A. Optical Properties of Aligned Rod-Shaped Gold Particles Dispersed in Poly(Vinyl Alcohol) Films. *J. Phys. Chem. B* **1999**, *103*, 5761−5767.
(41) Murphy, C. J.; Orendorff, C. J. Alignment of Gold Nanorods in Polymer Composites and on Polymer Surfaces. *Adv. Mater.* **2005**, *17*, 2173−2177.
(42) Pérez-Juste, J.; Rodríguez-González, B.; Mulvaney, P.; Liz-Marzán, L. M. Optical Control and Patterning of Gold-Nanorod−Poly(Vinyl Alcohol) Nanocomposite Films. *Adv. Funct. Mater.* **2005**, *15*, 1065−1071.
(43) Li, J.; Liu, S.; Liu, Y.; Zhou, F.; Li, Z.-Y. Anisotropic and Enhanced Absorptive Nonlinearities in a Macroscopic Film Induced by Aligned Gold Nanorods. *Appl. Phys. Lett.* **2010**, *96*, 263103.
(44) Roskov, K. E.; Kozek, K. A.; Wu, W.-C.; Chhetri, R. K.; Oldenburg, A. L.; Spontak, R. J.; Tracy, J. B. Long-Range Alignment of Gold Nanorods in Electrospun Polymer Nano/Microfibers. *Langmuir* **2011**, *27*, 13965−13969.
(45) Zhang, H.; Zhang, J.; Tong, X.; Ma, D.; Zhao, Y. Light Polarization-Controlled Shape-Memory Polymer/Gold Nanorod Composite. *Macromol. Rapid Commun.* **2013**, *34*, 1575−1579.
(46) Fornasiero, D.; Grieser, F. A Linear Dichroism Study of Colloidal Silver in Stretched Polymer Films. *Chem. Phys. Lett.* **1987**, *139*, 103−108.
(47) Dirix, Y.; Bastiaansen, C.; Caseri, W.; Smith, P. Oriented Pearl-Necklace Arrays of Metallic Nanoparticles in Polymers: A New Route

Toward Polarization-Dependent Color Filters. *Adv. Mater.* **1999**, *11*, 223−227.
(48) Pucci, A.; Bernabò, M.; Elvati, P.; Meza, L. I.; Galembeck, F.; de Paula Leite, C. A.; Tirelli, N.; Ruggeri, G. Photoinduced Formation of Gold Nanoparticles into Vinyl Alcohol Based Polymers. *J. Mater. Chem.* **2006**, *16*, 1058−1066.
(49) Uhlenhaut, D. I.; Smith, P.; Caseri, W. Color Switching in Gold—Polysiloxane Elastomeric Nanocomposites. *Adv. Mater.* **2006**, *18*, 1653−1656.
(50) Hribar, K. C.; Metter, R. B.; Ifkovits, J. L.; Troxler, T.; Burdick, J. A. Light-Induced Temperature Transitions in Biodegradable Polymer and Nanorod Composites. *Small* **2009**, *5*, 1830−1834.
(51) Zhang, H.; Xia, H.; Zhao, Y. Optically Triggered and Spatially Controllable Shape-Memory Polymer−Gold Nanoparticle Composite Materials. *J. Mater. Chem.* **2012**, *22*, 845−849.
(52) Xiao, Z.; Wu, Q.; Luo, S.; Zhang, C.; Baur, J.; Justice, R.; Liu, T. Shape Matters: A Gold Nanoparticle Enabled Shape Memory Polymer Triggered by Laser Irradiation. *Part. Part. Syst. Charact.* **2013**, *30*, 338−345.
(53) Zhang, H.; Zhao, Y. Polymers with Dual Light-Triggered Functions of Shape Memory and Healing Using Gold Nanoparticles. *ACS Appl. Mater. Interfaces* **2013**, *5*, 13069−13075.
(54) Leonardi, A. B.; Puig, J.; Antonacci, J.; Arenas, G. F.; Zucchi, I. A.; Hoppe, C. E.; Reven, L.; Zhu, L.; Toader, V.; Williams, R. J. J. Remote Activation by Green-Light Irradiation of Shape Memory Epoxies Containing Gold Nanoparticles. *Eur. Polym. J.* **2015**, *71*, 451−460.
(55) Yao, Y.; Hoang, P. T.; Liu, T. Laser Stimulated Shape Memory Polymer with Inclusion of Gold Nanorod—Effect of Aspect Ratio and Critical Role of On-resonance Irradiation. *J. Mater. Res. Technol.* **2017**, *33*, 869−873.
(56) Lu, X.; Zhang, H.; Fei, G.; Yu, B.; Tong, X.; Xia, H.; Zhao, Y. Liquid-Crystalline Dynamic Networks Doped with Gold Nanorods Showing Enhanced Photocontrol of Actuation. *Adv. Mater.* **2018**, *30*, 1706597.
(57) Hiramatsu, H.; Osterloh, F. E. A Simple Large-Scale Synthesis of Nearly Monodisperse Gold and Silver Nanoparticles with Adjustable Sizes and with Exchangeable Surfactants. *Chem. Mater.* **2004**, *16*, 2509−2511.
(58) Jie, Y.; Niskala, J. R.; Johnston-Peck, A. C.; Krommenhoek, P. J.; Tracy, J. B.; Fan, H.; You, W. Laterally Patterned Magnetic Nanoparticles. *J. Mater. Chem.* **2012**, *22*, 1962−1968.
(59) Mackay, M. E.; Tuteja, A.; Duxbury, P. M.; Hawker, C. J.; Van Horn, B.; Guan, Z.; Chen, G.; Krishnan, R. S. General Strategies for Nanoparticle Dispersion. *Science* **2006**, *311*, 1740−1743.
(60) Mangal, R.; Srivastava, S.; Archer, L. A. Phase Stability and Dynamics of Entangled Polymer−Nanoparticle Composites. *Nat. Commun.* **2015**, *6*, 7198.
(61) Kister, T.; Monego, D.; Mulvaney, P.; Widmer-Cooper, A.; Kraus, T. Colloidal Stability of Apolar Nanoparticles: The Role of Particle Size and Ligand Shell Structure. *ACS Nano* **2018**, *12*, 5969−5977.
(62) Takahashi, T.; Hayashi, N.; Hayashi, S. Structure and Properties of Shape-Memory Polyurethane Block Copolymers. *J. Appl. Polym. Sci.* **1996**, *60*, 1061−1069.
(63) Koerner, H.; Kelley, J. J.; Vaia, R. A. Transient Microstructure of Low Hard Segment Thermoplastic Polyurethane under Uniaxial Deformation. *Macromolecules* **2008**, *41*, 4709−4716.
(64) Baeza, G. P.; Genix, A.-C.; Degrandcourt, C.; Petitjean, L.; Gummel, J.; Couty, M.; Oberdisse, J. Multiscale Filler Structure in Simplified Industrial Nanocomposite Silica/SBR Systems Studied by SAXS and TEM. *Macromolecules* **2013**, *46*, 317−329.
(65) Harris, N.; Arnold, M. D.; Blaber, M. G.; Ford, M. J. Plasmonic Resonances of Closely Coupled Gold Nanosphere Chains. *J. Phys. Chem. C* **2009**, *113*, 2784−2791.
(66) Slaughter, L. S.; Wang, L.-Y.; Willingham, B. A.; Olson, J. M.; Swanglap, P.; Dominguez-Medina, S.; Link, S. Plasmonic Polymers Unraveled through Single Particle Spectroscopy. *Nanoscale* **2014**, *6*, 11451−11461.
(67) Mayer, M.; Schnepf, M. J.; König, T. A. F.; Fery, A. Colloidal Self-Assembly Concepts for Plasmonic Metasurfaces. *Adv. Opt. Mater.* **2019**, *7*, 1800564.
(68) Lioi, D. B.; Varshney, V.; Izor, S.; Neher, G.; Kennedy, W. J. Embedded Optical Nanosensors for Monitoring the Processing and Performance of Polymer Matrix Composites. *J. Mater. Chem. C* **2019**, *7*, 14471−14492.